Chemistry–A European Journal

Supporting Information

[$Ga^{3+}_{8}Sm^{3+}_{2}$, $Ga^{3+}_{8}Tb^{3+}_{2}$] Metallacrowns are Highly Promising Ratiometric Luminescent Molecular Nanothermometers Operating at Physiologically Relevant Temperatures

Elvin V. Salerno,[a] Justyna Zeler,[b, c] Svetlana V. Eliseeva,*[d] Miguel A. Hernández-Rodríguez,[b] Albano N. Carneiro Neto,[b] Stéphane Petoud,*[d] Vincent L. Pecoraro,*[a] and Luís D. Carlos*[b]

Contents

Experimental

Metallacrown synthesis. [MC:Sm] and [MC:Tb] were synthesized following the previously described procedure and correspond to the general composition $[Ga_8Ln_2(shi)_8(ip)_4(DMF)_2(H_2O)_2](NH_4^+)_2 \cdot 12DMF$ (Ln = Sm, Tb; where ip = $[isophthalate]^{2-}$, shi = $[salicylhydroxamate]^{3-}$).[1]

Encapsulation of [MC:Ln] in polystyrene beads. 100 nm diameter amino-functionalized polystyrene beads (PS/NH_2) were purchased from micromod Partikeltechnologie GmbH (Rostock, Germany). An encapsulation of [MC:Ln] inside PS/NH_2 beads was performed following a procedure that we have previously developed.[1] In general, a water suspension of PS/NH_2 beads (10 mg/mL, 300 µL) was mixed with solutions of either [MC:Sm], [MC:Tb] or [MC:Sm,Tb] (10 mM, 50 µL) dissolved in dimethylformamide (DMF) and vortexed for 1 hour. In the case of [MC:SmTb], the solution was prepared in 0.5 [MC:Sm] and 0.5 [MC:Tb] proportions. Next, 300 µL of water was added and the suspension was centrifuged (15200 rpm, 30 min). The supernatant was removed and [MC:Ln]@PS/NH_2 beads were washed with 300 µL of water three times and were finally resuspended in H_2O at a concentration of 10 mg/mL. Each washing step was accompanied by 30 min of sonication at room temperature. The supernatants collected after centrifugation and washings were checked by absorption spectroscopy and no detectable bands corresponding to [MC:Ln] absorption were observed indicating that the encapsulation step was complete.

Photoluminescence and Temperature Control. Emission and excitation spectra for the 10 mg/mL aqueous suspensions of [MC:Ln]@PS/NH_2 beads were recorded with a modular double grating excitation spectrofluorimeter with a TRIAX 320 emission monochromator (Fluorolog-3, Horiba Scientific) coupled to a R928 Hamamatsu photomultiplier using a front face configuration. A 450 W Xe arc lamp was used as the excitation source. Both emission and excitation spectra were corrected for the spectrofluorimeter optical spectral response and the spectral distribution of the lamp intensity using a photodiode reference detector, respectively. For the temperature-dependent (298-328 K) luminescence experiments performed on aqueous suspensions of [MC:Ln]@PS/NH_2 beads, the sample was in contact with a heating stage (Linkam, THMS 600).

For measurements of luminescence lifetimes, samples were placed into a closed-cycle Sumitomo cryostat (Janis Research CCS-500/204), while the temperature was controlled by a LakeShore temperature controller (Model 331). Luminescence lifetimes were determined under excitation at 355 nm provided by a Nd:YAG laser (YG 980; Quantel), the signals in the visible at 490 nm (Tb, $^5D_4$ level) and 702 nm (Sm, $^4G_{5/2}$ level) were detected by a Hamamatsu R928 PMT connected to

an iHR320 monochromator (Horiba Scientific). The output signals from the detector were fed into a 500 MHz bandpass digital oscilloscope (TDS 754C; Tektronix) and transferred to a PC for data processing using Origin 8® software. Luminescence lifetimes are averages of three independent measurements.

Repeatability. The repeatability of 10 mg/mL aqueous suspensions of [MC:Ln]@PS/NH_2 beads were estimated by cycling the temperature from 298 K up to 328 K, ensuring that each measurement is performed with the samples in thermal equilibrium with the temperature controller. The repeatability upon temperature cycling was quantified using the following expression:

$$R = 1 - \frac{\delta \Delta_m}{\bar{\Delta}} \quad \text{(S1)}$$

where $\delta\Delta_m$ is the maximum standard deviation in Δ and $\bar{\Delta}$ is the mean value of Δ during the temperature cycling. The precision of R is derived from $\delta\Delta_m$.

Theoretical

Ligand-to-Ln energy transfer

The intramolecular energy transfer (IET) rates were calculated taking into account the dipole–dipole (W_{d-d}), dipole–multipole (W_{d-m}), and exchange mechanisms (W_{ex}) in coordination compounds.[2–6] The coordination compounds herein analyzed are based on structural data and first excited states obtained from the experimental data. More details on the quantities in the equations below are in Refs. [2–8].

Eq. (S2) provides the dipole–dipole IET while the dipole–multipole ones (2^K-poles, $K = 2, 4$, and 6, respectively) is given by Eq. (S3):

$$W_{d-d} = \frac{S_L(1-\sigma_1)^2}{(2J+1)G}\frac{4\pi}{\hbar}\frac{e^2}{R_L^6}\sum_{\lambda}\Omega_K^{FED}\langle\psi^*J^*\|U^{(K)}\|\psi J\rangle^2 F \quad \text{(S2)}$$

$$W_{d-m} = \frac{S_L}{(2J+1)G}\frac{2\pi e^2}{\hbar}\sum_{K}(K+1)\frac{\langle r^K\rangle^2}{(R_L^{K+2})^2}\langle f\|C^{(K)}\|f\rangle^2(1-\sigma_K)^2\langle\psi^*J^*\|U^{(K)}\|\psi J\rangle^2 F \quad \text{(S3)}$$

where the intensity parameters Ω_K^{FED} are obtained by using only the forced electric dipole mechanism (Judd-Ofelt theory [9,10]). The sets of Ω_K^{FED} (in units of 10^{-20} cm^2) values were obtained using the Simple Overlap model [11,12] (considering the charge factors equal 1): Sm^{3+} $\{\Omega_2 = 0.056;\ \Omega_4 = 0.787;\ \Omega_6 = 1.379\}$ and Tb^{3+} $\{\Omega_2 = 0.028;\ \Omega_4 = 0.273;\ \Omega_6 = 0.458\}$.

S_L is the dipole strength of the ligand transition concerning IET, $\langle r^K\rangle$ are the 4*f* radial integrals, G is the ligand state degeneracy, R_L (5.98 Å) is the donor–acceptor states distance, $\langle f\|C^{(K)}\|f\rangle$ is the reduced matrix element of Racah's tensor operator, $(1-\sigma_K)$ are the shielding factors, and $\langle\psi^*J^*\|U^{(K)}\|\psi J\rangle^2$ are the squared reduced matrix elements from Carnall *et al.*[13].

The IET rate by the exchange interaction (Eq. S4) can be calculated by:

$$W_{ex} = \frac{\langle 4f|L\rangle^4}{(2J+1)}\frac{8\pi}{3\hbar}\frac{e^2}{R_L^4}\langle\psi^*J^*\|S\|\psi J\rangle^2\sum_{m}\left|\langle\phi|\sum_j\mu_z(j)s_m(j)\,|\phi^*\rangle\right|^2 F \quad \text{(S4)}$$

where $\langle 4f|L\rangle$ is the overlap integral between the ligand donor state and the 4*f* acceptor state at R_L distance, s_m the spin operator of electron j in the ligand, μ_z is the dipole operator (z-component), and $\langle\psi^*J^*\|S\|\psi J\rangle$ is the reduced matrix elements of the spin operator obtained using free-ion wavefunctions in the intermediate coupling scheme [14,15].

F (quantity in Eqs. S2, S3, and S4) is the energy mismatch condition which contains a sum over Franck-Condon factors.[3,6] In the case of IET involving lanthanide complex, F can be obtained by:

$$F = \frac{1}{\hbar\gamma_L}\sqrt{\frac{\ln(2)}{\pi}}\, e^{-\left(\frac{\Delta E}{\hbar\gamma_L}\right)^2 \ln(2)} \tag{S5}$$

Eq. (S5) can be assumed only when the corresponding bandwidth at half-height for the ligand (γ_L) is much larger than the lanthanide (γ_{Ln}) ion[6,16], $\gamma_L \gg \gamma_{Ln}$. Δ (in cm^{-1}) is the band maximum energy difference between ligand donor state and lanthanide ion acceptor state, $\Delta E = E_L - E_{Ln}$.

The forward IET for the *i*-th pathway (W_i) is calculated by the sum over all Eqs. (S2), (S3), and (S4):

$$W_i = W_{d-d} + W_{d-m} + W_{ex} \tag{S6}$$

The backward IET (W_i^b), that is, the energy returned from acceptor to donor state, is obtained with the same above equations, except for multiplying the energy mismatch factor F (Eq. (S5)) by the energy barrier factor $e^{-\left(\frac{|\Delta|}{k_b T}\right)}$, where k_b is the Boltzmann's constant in units of $cm^{-1}\cdot K^{-1}$. The IET values for [MC:Sm] and [MC:Tb] are presented in Table S7 and S8.

Ln-to-Ln energy transfer

The non-radiative energy transfer rates between lanthanide ions were calculated taking into account the dipole–dipole (W_{d-d}), the dipole–quadrupole (W_{d-q}), the quadrupole–quadrupole (W_{q-q}), and the exchange (W_{ex}) mechanisms [5]:

$$W_{d-d} = \frac{(1-\sigma_1^D)^2(1-\sigma_1^A)^2}{[J_D^*][J_A]}\frac{4\pi}{3\hbar}\frac{e^4}{{R_L}^6}\left(\sum_K \Omega_K^D \langle \psi_D J_D \| U^{(K)} \| \psi_D^* J_D^* \rangle^2\right) \times \\ \times \left(\sum_K \Omega_K^A \langle \psi_A^* J_A^* \| U^{(K)} \| \psi_A J_A \rangle^2\right) F \tag{S7}$$

$$W_{d-q,\ q-d} = \frac{\left(1-\sigma_1^{D,A}\right)^2\left(1-\sigma_2^{A,D}\right)^2}{[J_D^*][J_A]}\frac{\pi}{\hbar}\frac{e^4}{{R_L}^8}\langle f\|C^{(2)}\|f\rangle^2$$
$$\times\left[\left(\sum_K \Omega_K^D\,\langle\psi_D J_D\|U^{(K)}\|\psi_D^* J_D^*\rangle^2\right)\langle r^2\rangle_A^2\langle\psi_A^* J_A^*\|U^{(2)}\|\psi_A J_A\rangle^2\right. \quad \text{(S8)}$$
$$\left.+\left(\sum_K \Omega_K^A\,\langle\psi_A J_A\|U^{(K)}\|\psi_A^* J_A^*\rangle^2\right)\langle r^2\rangle_D^2\langle\psi_D^* J_D^*\|U^{(2)}\|\psi_D J_D\rangle^2\right]F$$

$$W_{q-q} = \frac{(1-\sigma_2^D)^2\left(1-\sigma_2^A\right)^2}{[J_D^*][J_A]}\frac{28\pi}{5\hbar}\frac{e^4}{{R_L}^{10}}\times\times\langle r^2\rangle_D^2\langle r^2\rangle_A^2\langle f\|C^{(2)}\|f\rangle^4\langle\psi_D J_D\|U^{(2)}\|\psi_D^* J_D^*\rangle^2 \quad \text{(S9)}$$
$$\times\langle\psi_A^* J_A^*\|U^{(2)}\|\psi_A J_A\rangle^2 F$$

$$W_{ex} = \frac{2\pi}{\hbar}\left[\left(\frac{e^2}{R_L}\right)\rho_{f-f}^2\right]^2 F \quad \text{(S10)}$$

where the intensity parameters Ω_K are the same obtained for the IET rates, once in Kushida's expressions the appearance of the Ω_K parameters is due to opposite parity configuration mixing, by the odd components of the ligand field, like in the Judd-Ofelt theory [17].

In Eq. (S10), ρ_{f-f} is the overlap integral between the 4*f* subshells of the donor and acceptor lanthanide ions. Figure S8 shows the behavior of the ρ_{f-f} with the distance of for the pair Tb–Sm. Each value was calculated with the ADF (Amsterdam Density Functional) program [18]. A DFT level of theory with the GGA BP86 functional [19,20] (Becke for the exchange and Perdew for the correlation effects), TZ2P Slater-Type basis set [21], and the inclusion of ZORA (zero-order regular approximation) scalar relativistic effects [22–24]. $\langle r^K\rangle$ are the 4*f* radial integrals [25].

In the case of energy transfer between two lanthanide ions the following analytical expression for F has been used [5]:

$$F = \frac{\ln(2)}{\sqrt{\pi}}\frac{1}{\hbar^2\gamma_D\gamma_A}\left\{\left[\left(\frac{1}{\hbar\gamma_D}\right)^2+\left(\frac{1}{\hbar\gamma_A}\right)^2\right]\ln(2)\right\}^{-\frac{1}{2}}$$
$$\times\exp\left[\frac{1}{4}\frac{\left(\frac{2\Delta E}{(\hbar\gamma_D)^2}\ln 2\right)^2}{\left[\left(\frac{1}{\hbar\gamma_A}\right)^2+\left(\frac{1}{\hbar\gamma_D}\right)^2\right]\ln 2}-\left(\frac{\Delta E}{\hbar\gamma_D}\right)^2\ln(2)\right] \quad \text{(S11)}$$

where $\hbar\gamma_D$ and $\hbar\gamma_A$ correspond to the bandwidths at half-height (in erg) of the donor and acceptor. For the present analysis, we considered $\gamma_D = \gamma_A = 400$ cm^{-1}. ΔE is the energy difference between donor and acceptor transitions, $\Delta E = E_D - E_A$.

The energy transfer mechanisms, pathways and their respective donor and acceptor states (Figure S9) were selected according to energy mismatch conditions and selection rules on the J quantum numbers. These selection rules are: for the multipolar mechanisms (W_{d-d}, W_{d-q} and W_{q-q}) $|J - J'| \leq K \leq J + J'$; for the exchange mechanism (W_{ex}) no defined selection rules on J appear.[26]

The energy transfer rates, in the same pathway, were calculated by the sum over Eqs. (S7)–(S10) $\left(W = W_{d-d} + W_{d-q} + W_{q-q} + W_{ex}\right)$ multiplying by the barrier factor if Δ is negative (Figure S9).

Since the [MC:Sm][MC:Tb] is a mixture of [MC:Sm] and [MC:Tb] samples, the shortest plausible distance Tb–Sm is $R_L = 12.82$ Å, coming from the closest intermolecular Ln^{3+}-Ln^{3+} distance in the Ln_2Ga_8 crystal structure.[27] The values of W at this distance are presented in Table S9 and Figure S10. The highest energy transfer rate is the $Tb^{3+}(^5D_4 \rightarrow {}^7F_6) \rightarrow Sm^{3+}(^6H_{5/2} \rightarrow {}^4I_{9/2})$ pathway with an inexpressive rate of 4.18×10^{-3} s^{-1}. For the sake of comparison, in a cubic system $Cs_2NaLnCl_6$ (Ln = Yb^{3+}, Er^{3+}) elpasolite, the energy transfer rate at the shortest Yb–Er distance (7.7 Å) is 2.15×10^{2} and 2.60×10^{2} s^{-1} (depending on the Er^{3+} acceptor levels) [28], five orders of magnitude higher than Tb–Sm rates in [MC:Sm][MC:Tb]. This supports the nullity of Tb^{3+}-Sm^{3+} energy transfer.

Figures

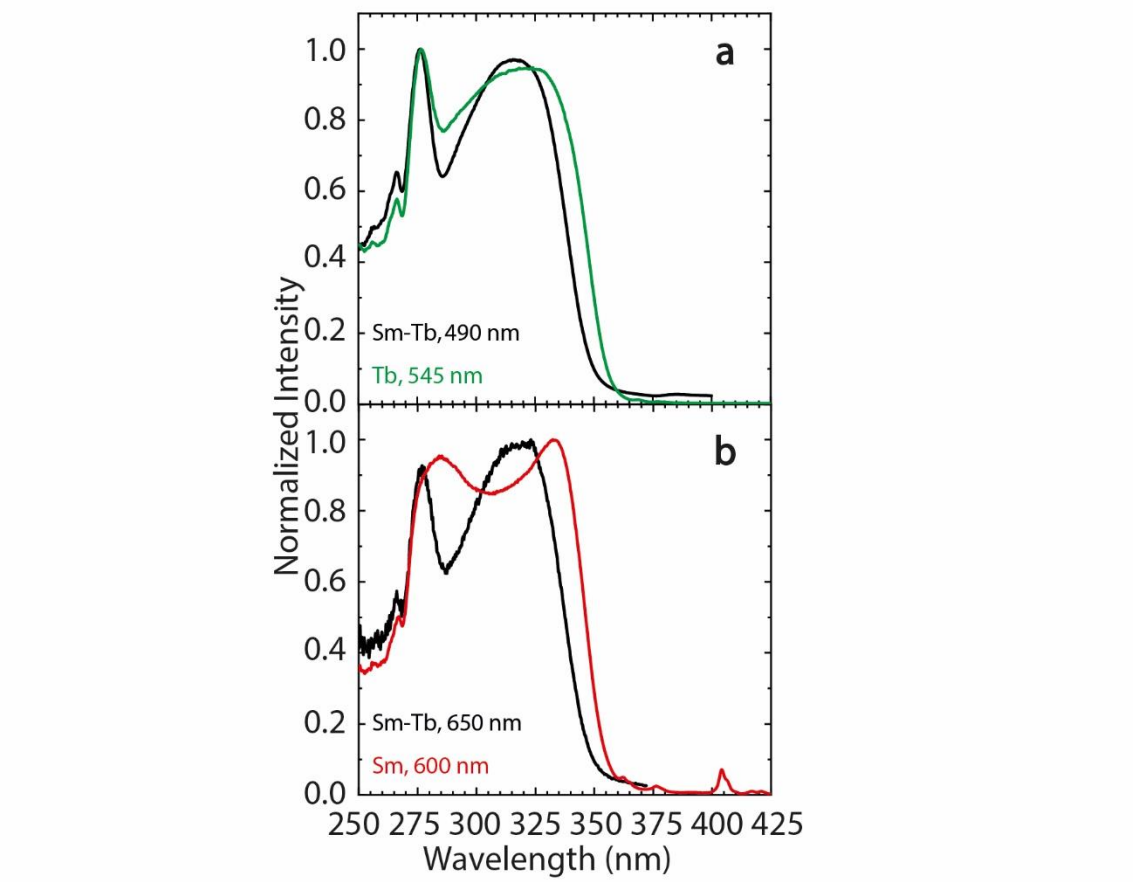

Figure S1. Excitation spectra of the 10 mg/mL aqueous suspension of [MC:Sm,Tb]@PS/NH_2, [MC:Tb]@PS/NH_2, and [MC:Sm]@PS/NH_2 beads while monitoring the main emission bands of the **(a)** Tb^{3+} and **(b)** Sm^{3+} cations at room temperature. The monitored wavelengths are indicated.

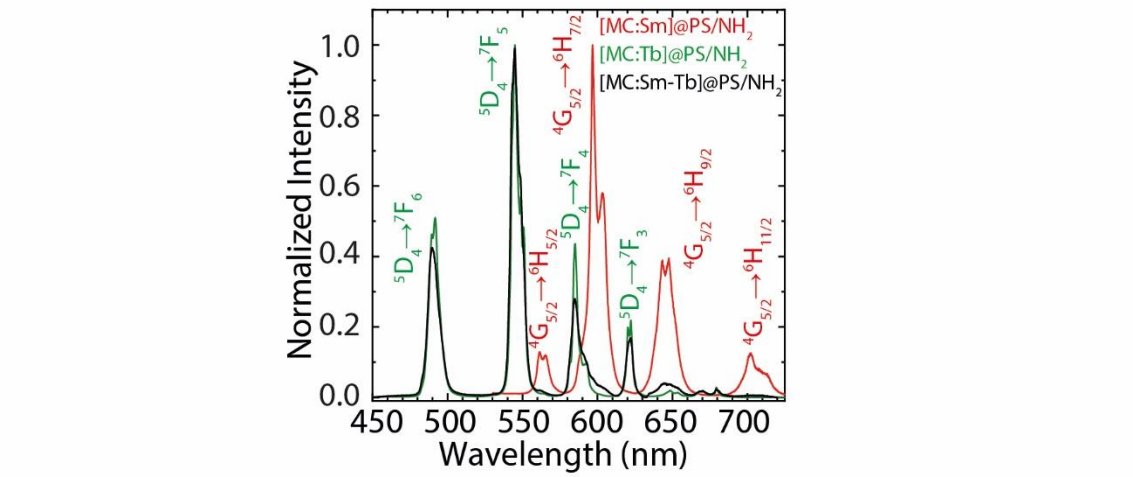

Figure S2. The normalized emission spectra of [MC:Sm]@PS/NH_2 , [MC:Tb]@PS/NH_2 and[MC:Sm,Tb]@PS/NH_2, under 340 nm excitation with indicated emission transitions of Sm^{3+} in red and Tb^{3+} in green.

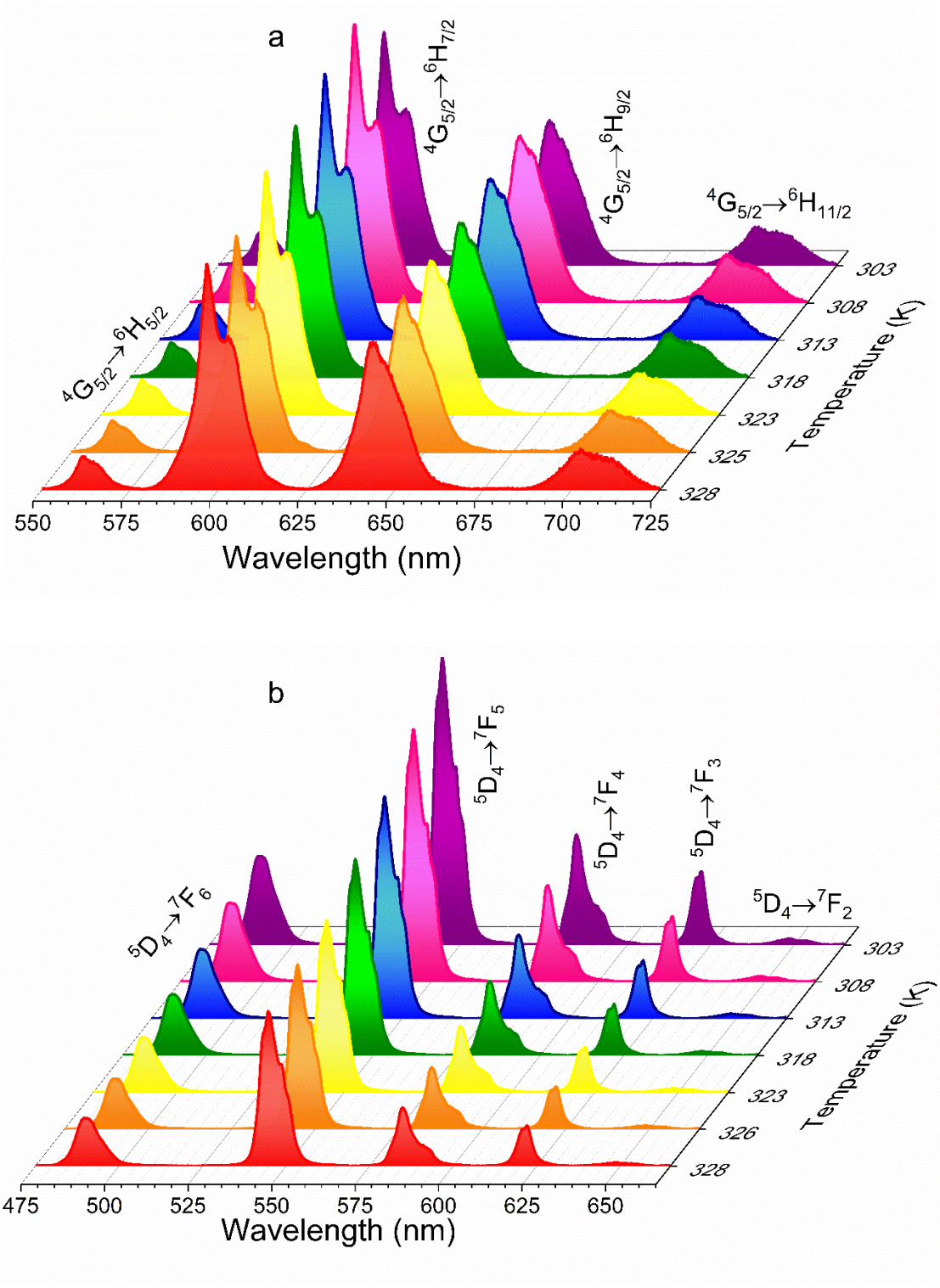

Figure S3. The temperature dependent emission spectra of a) [MC:Sm]@PS/NH_2 and b) [MC:Tb]@PS/NH_2 beads under 340 nm excitation.

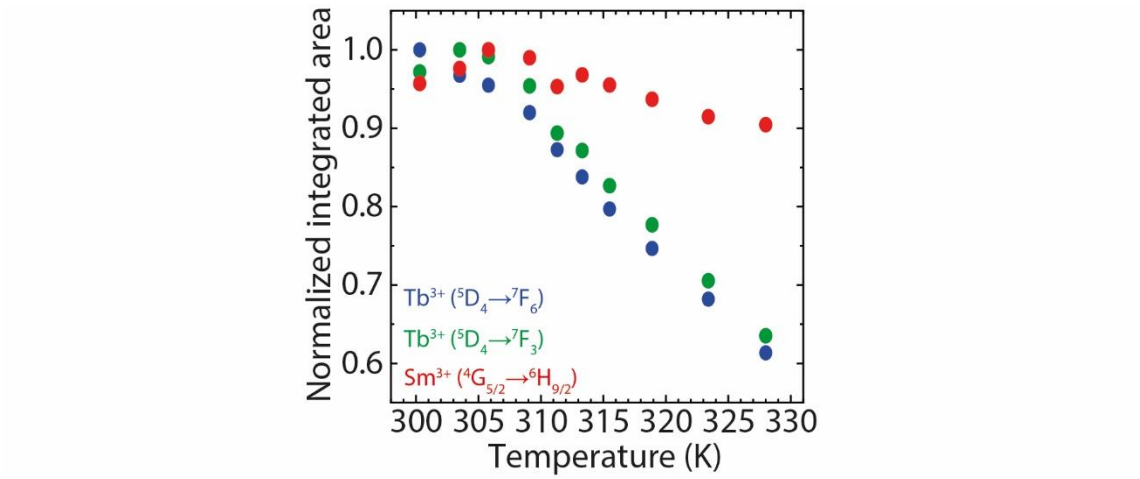

Figure S4. Luminescent behaviour of the 10 mg/mL aqueous suspension of [MC:Sm,Tb]@PS/NH_2 beads upon excitation at 340 nm at temperatures ranging from 298 K to 328 K.

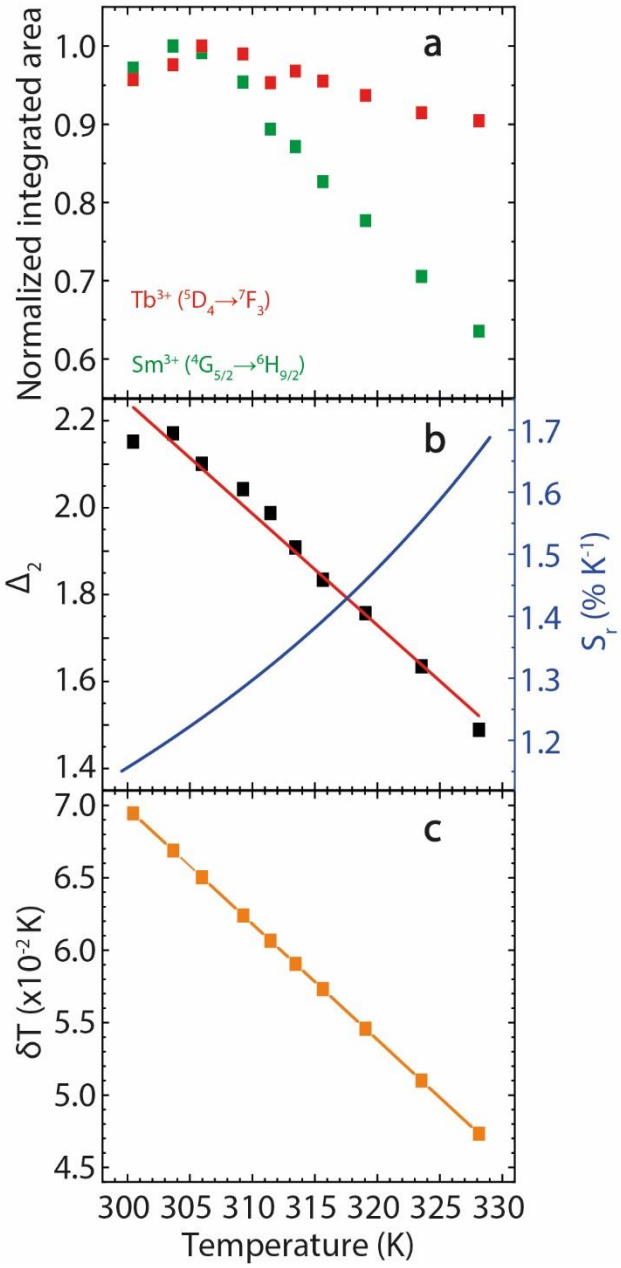

Figure S5. Thermometric behaviour of the 10 mg/mL aqueous suspension of [MC:Sm,Tb]@PS/NH_2 beads upon excitation at 340 nm in the temperature range 298 - 328 K. **(a)** Temperature evolution of the normalized integrated area of the emissions associated to Sm^{3+} ($^4G_{5/2}\rightarrow{}^6H_{9/2}$) (red) and Tb^{3+} ($^5D_4\rightarrow{}^7F_3$) (green) from 298 K to 328 K. **(b)** Ratio of the normalized integrated areas of the $^5D_4\rightarrow{}^7F_3/{}^4G_{5/2}\rightarrow{}^6H_{9/2}$ (Δ_2) transitions as well as its corresponding S_r (blue curve), obtained from the linear fits (red curve) of the experimental thermometric parameter. **(c)** The temperature uncertainty, δT, *vs.* temperature.

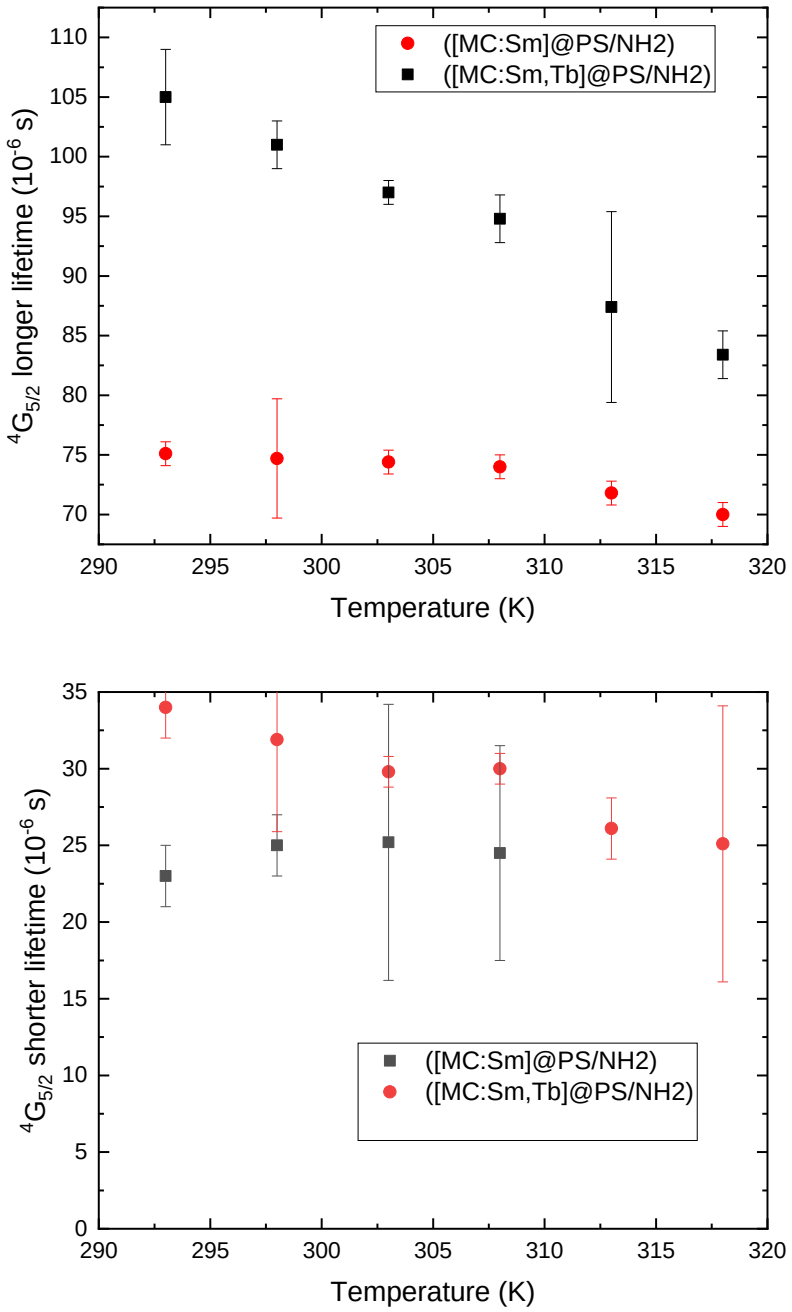

Figure S6. Luminescence lifetimes versus temperatures for the $^4G_{5/2}$ level in the mixed ([MC:Sm,Tb]@PS/NH_2) and pure ([MC:Sm]@PS/NH_2) samples. Longer component (τ_1), shorter component (τ_2) from Tables S3, S4.

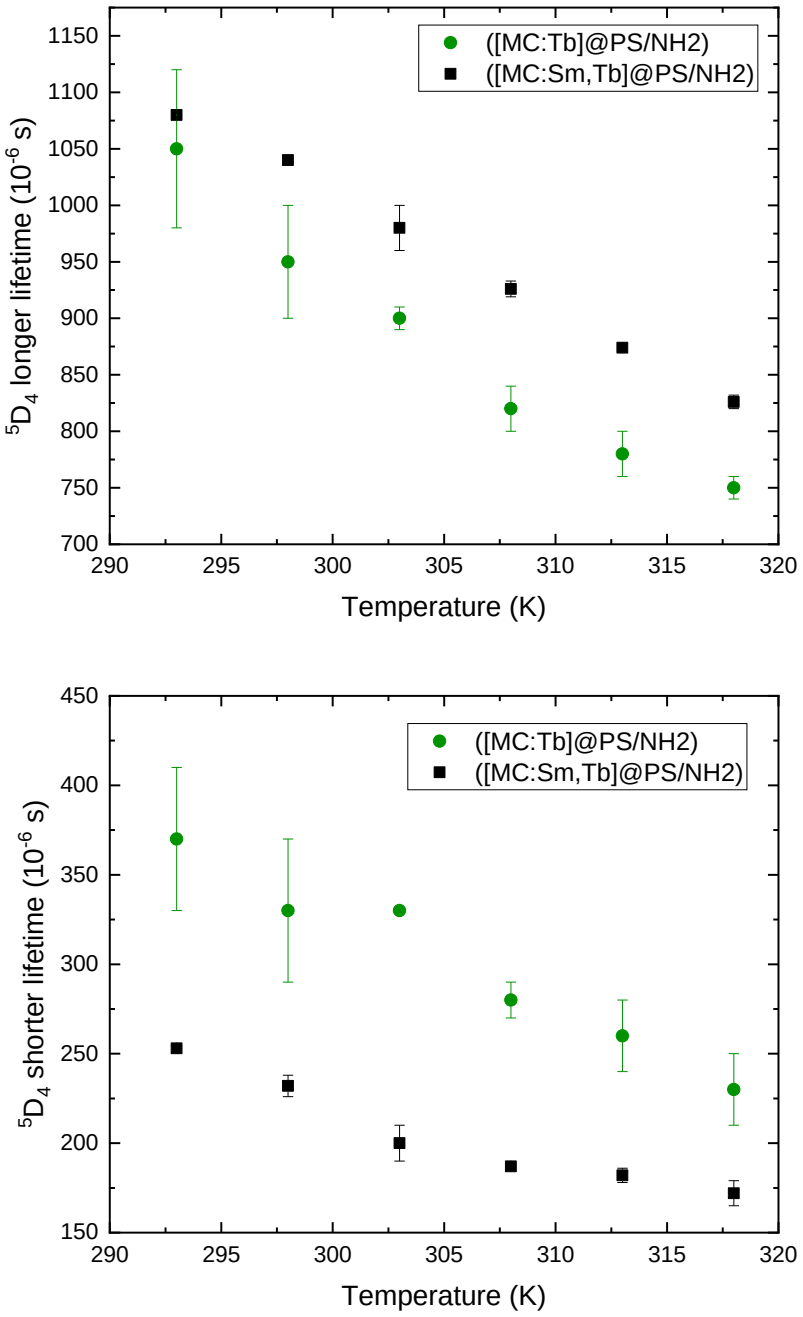

Figure S7. Luminescence lifetimes versus temperatures for the the $^5D_4$ level in the mixed ([MC:Sm,Tb]@PS/NH_2) and pure ([MC:Tb]@PS/NH_2) samples. Longer component (τ_1), shorter component (τ_2) from Tables S5, S6.

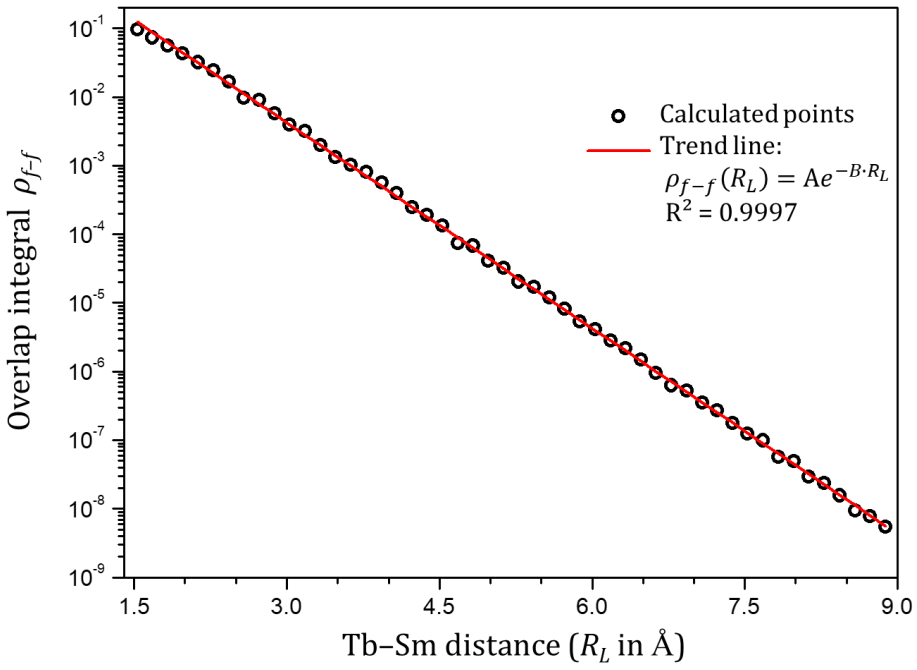

Figure S8. Log-linear graph of 4*f*-4*f* overlap integral (ρ_{f-f}) *versus* Tb–Sm distance (R_L). Each point was calculated with the ADF program [18] using a DFT level of theory (BP86 functional [19,20], TZ2P basis set [21], and the inclusion of ZORA scalar relativistic effects [22–24]). The trend line has as parameters $A = 4.176$ and $B = 2.299$.

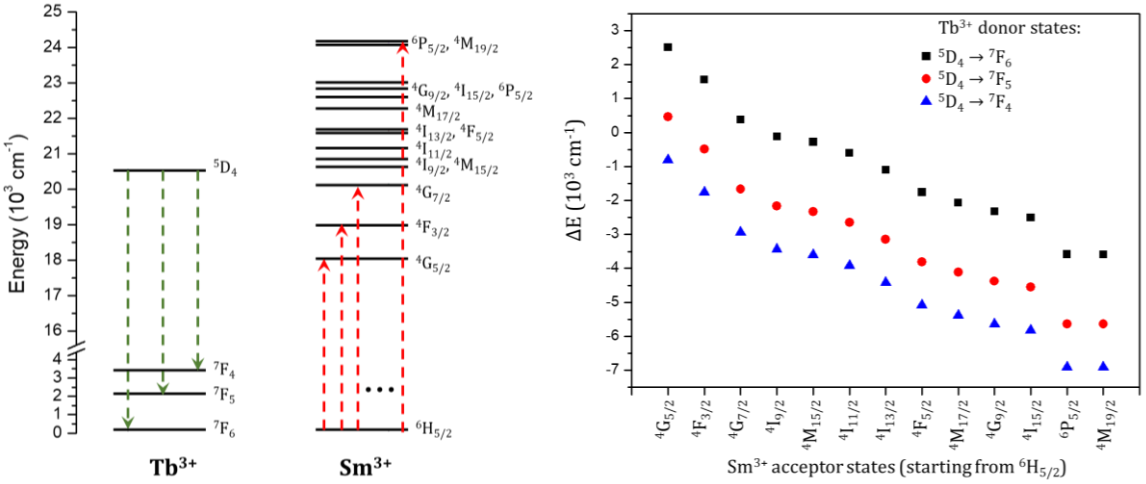

Figure S9. Schematic energy level diagram showing the energy levels of the donor (Tb^{3+}) and the acceptor (Sm^{3+}) involved in the energy transfer processes (left panel). The values of ΔE (used in Eq. (S11)) for the selected energy transfer pathways (right panel).

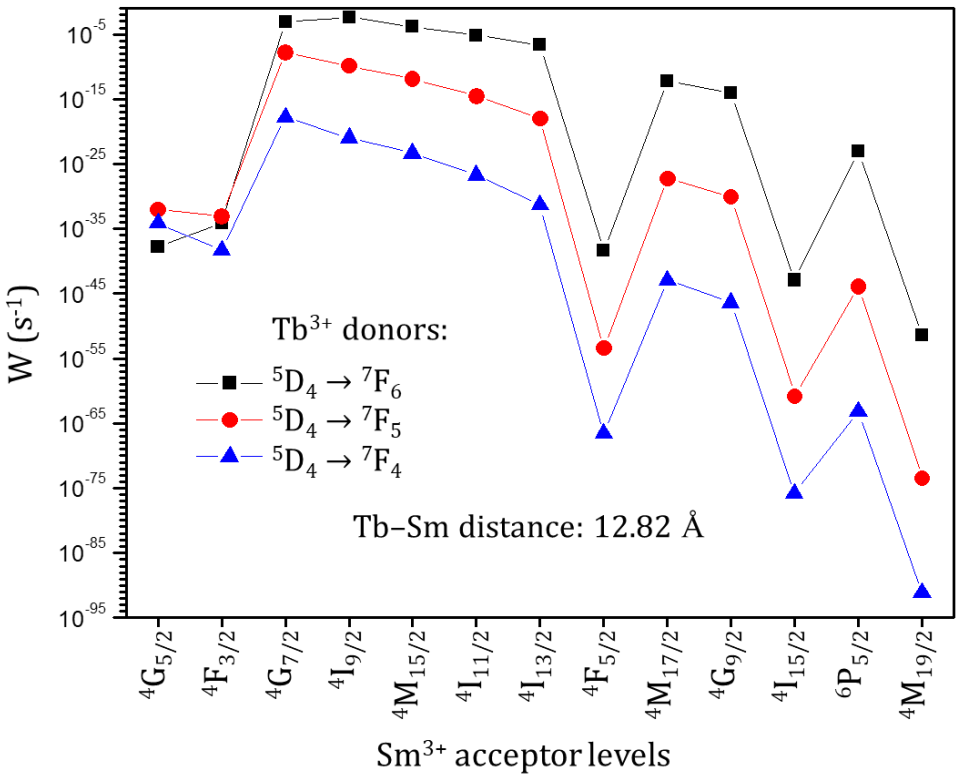

Figure S10. Log scale of the W values according to each pathway. The highest energy transfer rate is the $Tb^{3+}(^5D_4 \rightarrow {}^7F_6) \rightarrow Sm^{3+}(^6H_{5/2} \rightarrow {}^4I_{9/2})$ pathway with a rate of 4.18×10^{-3} s^{-1}. This only reinforces that the energy transfer between Tb^{3+} and Sm^{3+} ions can be neglected.

Tables

Table S1. Parameters of the $\Delta(T)$ calibration curves (straight lines) of the [MC:Sm,Tb]@PS/NH_2 beads. Ratios of the integrated areas of the $^5D_4 \rightarrow {}^7F_6$ (Tb^{3+})/$^4G_{5/2} \rightarrow {}^6H_{9/2}$ (Sm^{3+}) (Δ_1) and $^5D_4 \rightarrow {}^7F_3$ (Tb^{3+})/$^4G_{5/2} \rightarrow {}^6H_{9/2}$ (Sm^{3+}) (Δ_2) transitions were compared.

Thermometric parameter	Intercept	Slope	r^2
Δ_1	11.79±0.13	-0.109 ± 0.003	0.99
Δ_2	2.93±0.06	-0.026 ± 0.001	0.97

Table S2. Selected ratiometric Ln^{3+}-based luminescent nanothermometers. Excitation wavelength (λ_x), form of the samples, transitions involved, maximum relative sensitivity, S_m, in physiological range and the temperature (T_m) in which it occurs.

Optical sensor	Form	λ_x (nm)	Transitions	Physiological range (298-323 K)		References
				S_m (% K^{-1})	T_m (K)	
Er-Yb@LaF3:Yb-Tm nanoparticles[c]	Aqueous suspension	690	$^2F_{5/2} \rightarrow {}^2F_{7/2}$ $^4I_{13/2} \rightarrow {}^4I_{15/2}$	5	293	[29]
MOF: $Nd_{0.866}Yb_{0.134}BTB$[c]	Powder	808	$^2F_{5/2} \rightarrow {}^2F_{7/2}$ $^4F_{3/2} \rightarrow {}^4I_{11/2}$	4.755	333	[30]
$Eu_{0.058}Tb_{0.942}BPT$ [a]	Powder	325	$^5D_4 \rightarrow {}^7F_5$ $^5D_0 \rightarrow {}^7F_2$	2.3	323	[31]
[MC:Sm,Tb]@PS/NH_2 [b]	**Aqueous suspension**	**340**	**$^5D_4 \rightarrow {}^7F_6$** **$^4G_{5/2} \rightarrow {}^6H_{9/2}$**	**1.7**	**323**	**This work**
Eu^{3+}-Tb^{3+} functionalized SAM [b]	Powder	280	$^5D_4 \rightarrow {}^7F_5$ $^5D_0 \rightarrow {}^7F_2$	1.4	323	[32]
MOF-5: Eu^{3+}-Tb^{3+} [b]	Powder	325	$^5D_4 \rightarrow {}^7F_5$ $^5D_0 \rightarrow {}^7F_2$	0.7	323	[33]
LnMOF $Eu_{0.37}Tb_{0.63}$-BTC-a [b]	Powder	296	$^5D_4 \rightarrow {}^7F_5$ $^5D_0 \rightarrow {}^7F_2$	0.5	313	[34]
$Na[(Gd_{0.8}Eu_{0.1}Tb_{0.1})SiO_4]$ [c]	Powder	483.5	$^5D_4 \rightarrow {}^7F_5$ $^5D_0 \rightarrow {}^7F_2$	0.3	300	[35]
MOF: Tb^{3+}-Eu^{3+} [c]	Spray-dried	377	$^5D_4 \rightarrow {}^7F_5$ $^5D_0 \rightarrow {}^7F_2$	0.078	300	[36]

[a] Ligand-to-Ln^{3+} energy transfer. No information about temperature uncertainty is available.

[b] Ligand-to-Ln^{3+} energy transfer.

[c] Ln^{3+}-to-Ln^{3+} energy transfer.

Table S3. Observed luminescence lifetimes of the $^4G_{5/2}$ level (λ_{em} = 702 nm) for a 10 mg/mL suspension of 100 nm [MC:Sm]@PS/NH_2 beads in water upon excitation at 355 nm (2σ values between parentheses).

T (K)	τ_1 (µs)	B_1 (%)	τ_2 (µs)	B_2 (%)
293	75.1(1)	97.1(4)	23(2)	2.9(4)
298	74.7(5)	96.5(2)	25(2)	3.5(2)
303	74.4(1)	96.2(4)	25.2(9)	3.8(4)
308	74(1)	95.6(4)	24.5(7)	4.4(4)
313	71.8(1)	100		
318	70(1)	100		

Table S4. Observed luminescence lifetimes of the $^4G_{5/2}$ level (λ_{em} = 702 nm) for a 10 mg/mL suspension of 100 nm [MC:Sm,Tb]@PS/NH_2 beads in water upon excitation at 355 nm (2σ values between parentheses).

T (K)	τ_1 (µs)	B_1 (%)	τ_2 (µs)	B_2 (%)
293	105(4)	75.7(3)	34(2)	24.3(3)
298	101(2)	76.6(3)	31.9(6)	23.4(3)
303	97(1)	78.3(1)	29.8(1)	21.7(1)
308	94.8(2)	76(1)	30(1)	24(1)
313	87.4(8)	78.3(5)	26.1(2)	21.7(5)
318	83.4(2)	78(2)	25.1(9)	22(2)

Table S5. Observed luminescence lifetimes of the $^5D_4$ level (λ_{em} = 490 nm) for a 10 mg/mL suspension of 100 nm [MC:Tb]@PS/NH_2 beads in water upon excitation at 355 nm (2σ values between parentheses). Bi-exponential fit.

T (K)	τ_1 (µs)	B_1 (%)	τ_2 (µs)	B_2 (%)
293	950(50)	93(1)	178(9)	7(1)
298	840(30)	91(1)	164(1)	9(1)
303	770(30)	90(2)	149(2)	10(2)
308	700(30)	89(1)	136(3)	11(1)
313	640(20)	87(2)	121(3)	13(2)
318	580(20)	85(2)	105(7)	15(2)

Table S6. Observed luminescence lifetimes of the $^5D_4$ level (λ_{em} = 490 nm) for a 10 mg/mL suspension of 100 nm [MC:Sm,Tb]@PS/NH_2 beads in water upon excitation at 355 nm (2σ values between parentheses). Bi-exponential fit.

T (K)	τ_1 (μs)	B_1 (%)	τ_2 (μs)	B_2 (%)
293	830(10)	76.9(7)	142(7)	23.1(7)
298	813(7)	76.5(5)	134(5)	23.5(5)
303	775(1)	79.1(5)	107(3)	20.9(5)
308	751(4)	81.5(5)	94(4)	18.5(5)
313	707(7)	83.4(1)	81.8(8)	16.6(1)
318	668(3)	84.9(4)	72(1)	15.1(4)

Table S7. Forward and backward IET rates (in s^{-1}) for [MC:Sm], ΔE (in cm^{-1}) is the donor–acceptor energy difference and the predominant mechanism is shown in the last column. The most effective pathways and the total contribution (from S_1 and T_1) are highlighted in bold.

Pathway	Donor	Acceptor	ΔE	*W (forward)*	*W (backward)*	Mechanism
1	S_1	$^6H_{5/2} \rightarrow {}^4G_{5/2}$	13320	8.27×10^{5}	1.49×10^{-22}	exchange
2	S_1	$^6H_{5/2} \rightarrow {}^4F_{3/2}$	12369	0.00	0.00	dipole-dipole
3	S_1	$^6H_{5/2} \rightarrow {}^4G_{7/2}$	11190	5.72×10^{6}	2.82×10^{-17}	exchange
4	S_1	$^6H_{5/2} \rightarrow {}^4I_{9/2}$	10691	1.49×10^{4}	8.02×10^{-19}	dipole-multipole
5	S_1	$^6H_{5/2} \rightarrow {}^4M_{15/2}$	10526	1.06×10^{3}	1.27×10^{-19}	dipole-dipole
6	S_1	$^6H_{5/2} \rightarrow {}^4I_{11/2}$	10204	4.91×10^{2}	2.74×10^{-19}	dipole-dipole
7	S_1	$^6H_{5/2} \rightarrow {}^4I_{13/2}$	9707	1.79×10^{3}	1.08×10^{-17}	dipole-dipole
8	S_1	$^6H_{5/2} \rightarrow {}^4F_{5/2}$	9050	5.18×10^{7}	7.33×10^{-12}	exchange
9	S_1	$^6H_{5/2} \rightarrow {}^4M_{17/2}$	8739	7.94×10^{2}	4.99×10^{-16}	dipole-dipole
10	S_1	$^6H_{5/2} \rightarrow {}^4G_{9/2}$	8478	6.14×10^{2}	1.35×10^{-15}	dipole-dipole
11	S_1	$^6H_{5/2} \rightarrow {}^4L_{13/2}$	6675	9.18×10^{3}	1.15×10^{-10}	dipole-dipole
12	S_1	$^6H_{5/2} \rightarrow {}^4F_{7/2}$	6356	1.32×10^{8}	7.60×10^{-6}	exchange
13	S_1	$^6H_{5/2} \rightarrow {}^6P_{3/2}$	6287	9.65×10^{4}	7.75×10^{-9}	dipole-dipole
14	S_1	$^6H_{5/2} \rightarrow {}^4K_{11/2}$	6150	2.13×10^{3}	3.30×10^{-10}	dipole-dipole
15	S_1	$^6H_{5/2} \rightarrow {}^4L_{15/2}$	5684	5.56×10^{3}	8.05×10^{-9}	dipole-dipole
16	S_1	$^6H_{5/2} \rightarrow {}^4G_{11/2}$	5522	1.16×10^{3}	3.66×10^{-9}	dipole-dipole
17	**S_1**	**$^6H_{5/2} \rightarrow {}^6P_{7/2}$**	**4565**	$\mathbf{1.20\times10^{9}}$	$\mathbf{3.73\times10^{-1}}$	**exchange**
		Total contribution from S_1		$\boldsymbol{1.39\times10^{9}}$	$\boldsymbol{3.73\times10^{-1}}$	
18	**T_1**	**$^6H_{5/2} \rightarrow {}^4G_{5/2}$**	**4050**	$\mathbf{1.90\times10^{10}}$	$\mathbf{6.96\times10^{1}}$	**exchange**
19	T_1	$^6H_{5/2} \rightarrow {}^4F_{3/2}$	3099	0.00	0.00	dipole-dipole
20	T_1	$^6H_{5/2} \rightarrow {}^4G_{7/2}$	1920	3.69×10^{8}	3.69×10^{4}	exchange
21	T_1	$^6H_{5/2} \rightarrow {}^4I_{9/2}$	1421	7.24×10^{1}	7.94×10^{-2}	dipole-multipole
22	T_1	$^6H_{5/2} \rightarrow {}^4M_{15/2}$	1256	4.00	9.67×10^{-3}	dipole-dipole
23	T_1	$^6H_{5/2} \rightarrow {}^4I_{11/2}$	934	1.43	1.63×10^{-2}	dipole-dipole
24	T_1	$^6H_{5/2} \rightarrow {}^4I_{13/2}$	437	3.52	4.33×10^{-1}	dipole-dipole
25	T_1	$^6H_{5/2} \rightarrow {}^4F_{5/2}$	-220	7.26×10^{7}	2.09×10^{8}	exchange
26	T_1	$^6H_{5/2} \rightarrow {}^4M_{17/2}$	-531	4.39×10^{-3}	5.60×10^{-2}	dipole-dipole
27	T_1	$^6H_{5/2} \rightarrow {}^4G_{9/2}$	-792	2.29×10^{-4}	1.02×10^{-2}	dipole-dipole
28	T_1	$^6H_{5/2} \rightarrow {}^4L_{13/2}$	-2595	2.44×10^{-11}	6.20×10^{-6}	dipole-dipole
		Total contribution from T_1		$\boldsymbol{1.94\times10^{10}}$	$\boldsymbol{2.09\times10^{8}}$	

Table S8. Forward and backward IET rates (in s^{-1}) for [MC:Tb], ΔE (in cm^{-1}) is the donor–acceptor energy difference and the predominant mechanism is shown in the last column. The most effective pathways and the total contribution (from S_1 and T_1) are highlighted in bold.

Pathway	Donor	Acceptor	ΔE	*W (forward)*	*W (backward)*	Mechanism
1	**S_1**	**$^7F_6 \rightarrow {}^5L_6$**	**1640**	**4.27×10^5**	**1.64×10^2**	**exchange**
2	**S_1**	**$^7F_6 \rightarrow {}^5H_7$**	**-129**	**2.87×10^5**	**5.32×10^5**	**exchange**
3	S_1	$^7F_6 \rightarrow {}^5H_6$	-1641	1.46×10^3	3.82×10^6	exchange
4	S_1	$^7F_6 \rightarrow {}^5H_5$	-2517	0.00	0.00	dipole-dipole
5	S_1	$^7F_6 \rightarrow {}^5F_5$	-3684	1.03×10^{-1}	4.87×10^6	exchange
6	S_1	$^7F_5 \rightarrow {}^5L_6$	3688	4.27×10^4	8.90×10^{-4}	exchange
7	S_1	$^7F_5 \rightarrow {}^5H_7$	1919	0.00	0.00	dipole-dipole
8	**S_1**	**$^7F_5 \rightarrow {}^5H_6$**	**407**	**6.50×10^5**	**9.23×10^4**	**exchange**
9	**S_1**	**$^7F_5 \rightarrow {}^5H_5$**	**-469**	**8.51×10^5**	**8.07×10^6**	**exchange**
10	S_1	$^7F_5 \rightarrow {}^5F_5$	-1636	3.18×10^3	8.12×10^6	exchange
		Total contribution from S_1		**2.26×10^6**	**2.55×10^7**	
11	T_1	$^7F_6 \rightarrow {}^5D_4$	1536	9.60	6.07×10^{-3}	dipole-multipole
12	T_1	$^7F_6 \rightarrow {}^5D_3$	-4256	2.07×10^{-11}	1.52×10^{-2}	dipole-dipole
13	**T_1**	**$^7F_6 \rightarrow {}^5G_6$**	**-4443**	**2.33×10^{-3}**	**4.19×10^6**	**exchange**
14	T_1	$^7F_6 \rightarrow {}^5L_{10}$	-4991	1.64×10^{-11}	4.08×10^{-1}	dipole-dipole
15	T_1	$^7F_6 \rightarrow {}^5G_5$	-5787	1.40×10^{-7}	1.58×10^5	exchange
16	T_1	$^7F_6 \rightarrow {}^5G_4$	-6307	1.78×10^{-14}	2.43×10^{-1}	dipole-multipole
17	T_1	$^7F_5 \rightarrow {}^5D_4$	3584	6.14×10^5	2.10×10^{-2}	exchange
18	T_1	$^7F_5 \rightarrow {}^5D_3$	-2208	1.44×10^{-4}	5.72	dipole-multipole
19	**T_1**	**$^7F_5 \rightarrow {}^5G_6$**	**-2395**	**1.22×10^1**	**1.19×10^6**	**exchange**
20	T_1	$^7F_5 \rightarrow {}^5L_{10}$	-2943	1.86×10^{-8}	2.50×10^{-2}	dipole-dipole
21	**T_1**	**$^7F_5 \rightarrow {}^5G_5$**	**-3739**	**4.53×10^{-2}**	**2.78×10^6**	**exchange**
22	T_1	$^7F_5 \rightarrow {}^5G_4$	-4259	3.94×10^{-4}	2.93×10^5	exchange
		Total contribution from T_1		***6.14×10^5***	***8.61×10^6***	

Table S9. Energy transfer rates (s^{-1}) from Tb^{3+} to Sm^{3+} for each mechanism using the crystallographic closest distance $R_L = 12.82$ Å. W is the sum over all mechanisms considering the barrier factor (if applicable). One should notice that the energy transfer $Tb^{3+}(^5D_4 \rightarrow {}^7F_6) \rightarrow Sm^{3+}(^6H_{5/2} \rightarrow {}^4I_{9/2})$ has the highest contribution (pathway 4, highlighted in bold).

Pathway Label	Donor	Acceptor	W_{d-d}	W_{d-q}	W_{q-q}	W_{ex}	W
1	$^5D_4 \rightarrow {}^7F_6$	$^6H_{5/2} \rightarrow {}^4G_{5/2}$	0.00	0.00	0.00	1.72×10^{-38}	1.72×10^{-38}
2	$^5D_4 \rightarrow {}^7F_6$	$^6H_{5/2} \rightarrow {}^4F_{3/2}$	0.00	0.00	0.00	7.63×10^{-35}	7.63×10^{-35}
3	$^5D_4 \rightarrow {}^7F_6$	$^6H_{5/2} \rightarrow {}^4G_{7/2}$	2.47×10^{-6}	5.74×10^{-5}	7.31×10^{-4}	1.10×10^{-32}	7.90×10^{-4}
4	**$^5D_4 \rightarrow {}^7F_6$**	**$^6H_{5/2} \rightarrow {}^4I_{9/2}$**	**1.79×10^{-6}**	**8.31×10^{-5}**	**7.16×10^{-3}**	**1.47×10^{-32}**	**4.18×10^{-3}**
5	$^5D_4 \rightarrow {}^7F_6$	$^6H_{5/2} \rightarrow {}^4M_{15/2}$	2.79×10^{-5}	5.96×10^{-4}	0.00	1.28×10^{-32}	1.63×10^{-4}
6	$^5D_4 \rightarrow {}^7F_6$	$^6H_{5/2} \rightarrow {}^4I_{11/2}$	5.25×10^{-6}	1.12×10^{-4}	0.00	6.92×10^{-33}	6.54×10^{-6}
7	$^5D_4 \rightarrow {}^7F_6$	$^6H_{5/2} \rightarrow {}^4I_{13/2}$	1.93×10^{-6}	4.13×10^{-5}	0.00	1.11×10^{-33}	2.22×10^{-7}
8	$^5D_4 \rightarrow {}^7F_6$	$^6H_{5/2} \rightarrow {}^4F_{5/2}$	0.00	0.00	0.00	1.91×10^{-35}	4.19×10^{-39}
9	$^5D_4 \rightarrow {}^7F_6$	$^6H_{5/2} \rightarrow {}^4M_{17/2}$	5.35×10^{-10}	1.14×10^{-8}	0.00	1.45×10^{-36}	5.93×10^{-13}
10	$^5D_4 \rightarrow {}^7F_6$	$^6H_{5/2} \rightarrow {}^4G_{9/2}$	2.66×10^{-11}	5.67×10^{-10}	0.00	1.21×10^{-37}	8.41×10^{-15}
11	$^5D_4 \rightarrow {}^7F_6$	$^6H_{5/2} \rightarrow {}^4I_{15/2}$	0.00	0.00	0.00	1.94×10^{-38}	1.19×10^{-43}
12	$^5D_4 \rightarrow {}^7F_6$	$^6H_{5/2} \rightarrow {}^6P_{5/2}$	1.14×10^{-17}	2.43×10^{-16}	0.00	1.19×10^{-44}	8.58×10^{-24}
13	$^5D_4 \rightarrow {}^7F_6$	$^6H_{5/2} \rightarrow {}^4M_{19/2}$	0.00	0.00	0.00	1.09×10^{-44}	3.57×10^{-52}
14	$^5D_4 \rightarrow {}^7F_5$	$^6H_{5/2} \rightarrow {}^4G_{5/2}$	0.00	0.00	0.00	9.48×10^{-33}	9.48×10^{-33}
15	$^5D_4 \rightarrow {}^7F_5$	$^6H_{5/2} \rightarrow {}^4F_{3/2}$	0.00	0.00	0.00	9.11×10^{-33}	8.90×10^{-34}
16	$^5D_4 \rightarrow {}^7F_5$	$^6H_{5/2} \rightarrow {}^4G_{7/2}$	1.77×10^{-8}	2.88×10^{-6}	3.94×10^{-5}	3.77×10^{-35}	1.45×10^{-8}
17	$^5D_4 \rightarrow {}^7F_5$	$^6H_{5/2} \rightarrow {}^4I_{9/2}$	1.53×10^{-10}	2.85×10^{-8}	4.62×10^{-6}	6.02×10^{-37}	1.45×10^{-10}
18	$^5D_4 \rightarrow {}^7F_5$	$^6H_{5/2} \rightarrow {}^4M_{15/2}$	5.53×10^{-10}	8.88×10^{-8}	0.00	1.21×10^{-37}	1.27×10^{-12}
19	$^5D_4 \rightarrow {}^7F_5$	$^6H_{5/2} \rightarrow {}^4I_{11/2}$	5.97×10^{-12}	9.60×10^{-10}	0.00	3.76×10^{-39}	2.92×10^{-15}
20	$^5D_4 \rightarrow {}^7F_5$	$^6H_{5/2} \rightarrow {}^4I_{13/2}$	2.68×10^{-14}	4.30×10^{-12}	0.00	7.32×10^{-42}	1.21×10^{-18}
21	$^5D_4 \rightarrow {}^7F_5$	$^6H_{5/2} \rightarrow {}^4F_{5/2}$	0.00	0.00	0.00	3.70×10^{-46}	4.42×10^{-54}
22	$^5D_4 \rightarrow {}^7F_5$	$^6H_{5/2} \rightarrow {}^4M_{17/2}$	1.38×10^{-21}	2.22×10^{-19}	0.00	1.78×10^{-48}	6.00×10^{-28}
23	$^5D_4 \rightarrow {}^7F_5$	$^6H_{5/2} \rightarrow {}^4G_{9/2}$	6.76×10^{-24}	1.09×10^{-21}	0.00	1.47×10^{-50}	8.40×10^{-31}
24	$^5D_4 \rightarrow {}^7F_5$	$^6H_{5/2} \rightarrow {}^4I_{15/2}$	0.00	0.00	0.00	4.98×10^{-52}	1.65×10^{-61}
25	$^5D_4 \rightarrow {}^7F_5$	$^6H_{5/2} \rightarrow {}^6P_{5/2}$	4.08×10^{-35}	6.55×10^{-33}	0.00	2.04×10^{-62}	1.21×10^{-44}
26	$^5D_4 \rightarrow {}^7F_5$	$^6H_{5/2} \rightarrow {}^4M_{19/2}$	0.00	0.00	0.00	1.76×10^{-62}	3.14×10^{-74}
27	$^5D_4 \rightarrow {}^7F_4$	$^6H_{5/2} \rightarrow {}^4G_{5/2}$	0.00	0.00	0.00	3.78×10^{-33}	8.11×10^{-35}
28	$^5D_4 \rightarrow {}^7F_4$	$^6H_{5/2} \rightarrow {}^4F_{3/2}$	0.00	0.00	0.00	1.96×10^{-35}	4.41×10^{-39}
29	$^5D_4 \rightarrow {}^7F_4$	$^6H_{5/2} \rightarrow {}^4G_{7/2}$	4.19×10^{-14}	2.12×10^{-13}	1.85×10^{-12}	1.26×10^{-40}	1.65×10^{-18}
30	$^5D_4 \rightarrow {}^7F_4$	$^6H_{5/2} \rightarrow {}^4I_{9/2}$	2.34×10^{-17}	6.63×10^{-16}	1.40×10^{-14}	1.30×10^{-43}	1.06×10^{-21}
31	$^5D_4 \rightarrow {}^7F_4$	$^6H_{5/2} \rightarrow {}^4M_{15/2}$	3.42×10^{-17}	1.09×10^{-16}	0.00	1.05×10^{-44}	4.66×10^{-24}
32	$^5D_4 \rightarrow {}^7F_4$	$^6H_{5/2} \rightarrow {}^4I_{11/2}$	6.30×10^{-20}	2.01×10^{-19}	0.00	5.59×10^{-47}	1.83×10^{-27}
33	$^5D_4 \rightarrow {}^7F_4$	$^6H_{5/2} \rightarrow {}^4I_{13/2}$	1.85×10^{-23}	5.89×10^{-23}	0.00	7.12×10^{-51}	4.96×10^{-32}
34	$^5D_4 \rightarrow {}^7F_4$	$^6H_{5/2} \rightarrow {}^4F_{5/2}$	0.00	0.00	0.00	9.78×10^{-57}	2.68×10^{-67}
35	$^5D_4 \rightarrow {}^7F_4$	$^6H_{5/2} \rightarrow {}^4M_{17/2}$	4.69×10^{-33}	1.50×10^{-32}	0.00	8.55×10^{-60}	1.21×10^{-43}
36	$^5D_4 \rightarrow {}^7F_4$	$^6H_{5/2} \rightarrow {}^4G_{9/2}$	5.48×10^{-36}	1.75×10^{-35}	0.00	1.68×10^{-62}	4.05×10^{-47}
37	$^5D_4 \rightarrow {}^7F_4$	$^6H_{5/2} \rightarrow {}^4I_{15/2}$	0.00	0.00	0.00	2.18×10^{-64}	1.66×10^{-76}
38	$^5D_4 \rightarrow {}^7F_4$	$^6H_{5/2} \rightarrow {}^6P_{5/2}$	3.30×10^{-50}	1.05×10^{-49}	0.00	2.33×10^{-77}	5.82×10^{-64}
39	$^5D_4 \rightarrow {}^7F_4$	$^6H_{5/2} \rightarrow {}^4M_{19/2}$	0.00	0.00	0.00	1.95×10^{-77}	7.96×10^{-92}
					Total Tb-Sm energy transfer		**5.14×10^{-3}**

References

[1] I. Martinić, S. V. Eliseeva, G. Collet, T. Y. Luo, N. Rosi, S. Petoud, *ACS Appl. Bio Mater.* **2019**, *2*, 1667–1675.

[2] O. L. Malta, *J. Lumin.* **1997**, *71*, 229–236.

[3] O. L. Malta, F. R. Gonçalves e Silva, *Spectrochim. Acta Part A Mol. Biomol. Spectrosc.* **1998**, *54*, 1593–1599.

[4] R. Longo, F. R. Gonçalves e Silva, O. L. Malta, *Chem. Phys. Lett.* **2000**, *328*, 67–74.

[5] O. L. Malta, *J. Non. Cryst. Solids* **2008**, *354*, 4770–4776.

[6] A. N. Carneiro Neto, E. E. S. Teotonio, G. F. de Sá, H. F. Brito, J. Legendziewicz, L. D. Carlos, M. C. F. C. Felinto, P. Gawryszewska, R. T. Moura Jr., R. L. Longo, et al., in *Handb. Phys. Chem. Rare Earths* (Eds.: J.-C.G. Bünzli, V.K. Pecharsky), Elsevier, Amsterdam, **2019**, pp. 55–162.

[7] F. R. G. e Silva, O. L. Malta, *J. Alloys Compd.* **1997**, *250*, 427–430.

[8] H. F. Brito, O. M. L. Malta, M. C. F. C. Felinto, E. E. S. Teotonio, in *Chem. Met. Enolates* (Ed.: J. Zabicky), Wiley-VCH Verlag GmbH, Weinheim, Germany, **2009**, pp. 131–177.

[9] B. R. Judd, *Phys. Rev.* **1962**, *127*, 750–761.

[10] G. S. Ofelt, *J. Chem. Phys.* **1962**, *37*, 511–520.

[11] O. L. Malta, *Chem. Phys. Lett.* **1982**, *88*, 353–356.

[12] O. L. Malta, *Chem. Phys. Lett.* **1982**, *87*, 27–29.

[13] W. T. Carnall, H. Crosswhite, H. M. Crosswhite, *Energy Level Structure and Transition Probabilities in the Spectra of the Trivalent Lanthanides in LaF_3*, Argonne, IL, United States, **1978**.

[14] G. S. Ofelt, *J. Chem. Phys.* **1963**, *38*, 2171–2180.

[15] E. Kasprzycka, A. N. Carneiro Neto, V. A. Trush, L. Jerzykiewicz, V. M. Amirkhanov, O. L. Malta, J. Legendziewicz, P. Gawryszewska, *J. Rare Earths* **2020**, *38*, 552–563.

[16] O. L. Malta, H. F. Brito, J. F. S. Menezes, F. R. G. e Silva, S. Alves, F. S. Farias, A. V. M. de Andrade, *J. Lumin.* **1997**, *75*, 255–268.

[17] T. Kushida, *J. Phys. Soc. Japan* **1973**, *34*, 1318–1326.

[18] G. te Velde, F. M. Bickelhaupt, E. J. Baerends, C. Fonseca Guerra, S. J. A. van Gisbergen, J. G. Snijders, T. Ziegler, *J. Comput. Chem.* **2001**, *22*, 931–967.

[19] A. D. Becke, *Phys. Rev. A* **1988**, *38*, 3098–3100.

[20] J. P. Perdew, *Phys. Rev. B* **1986**, *33*, 8822–8824.

[21] E. Van Lenthe, E. J. Baerends, *J. Comput. Chem.* **2003**, *24*, 1142–1156.

[22] E. Van Lenthe, J. G. Snijders, E. J. Baerends, *J. Chem. Phys.* **1996**, *105*, 6505–6516.

[23] E. Van Lenthe, E. J. Baerends, J. G. Snijders, *J. Chem. Phys.* **1994**, *101*, 9783–9792.

[24] E. Van Lenthe, *J. Chem. Phys.* **1999**, *110*, 8943–8953.

[25] S. Edvardsson, M. Klintenberg, *J. Alloys Compd.* **1998**, *275–277*, 230–233.

[26] A. N. Carneiro Neto, R. T. Moura Jr, A. Shyichuk, V. Paterlini, F. Piccinelli, M. Bettinelli, O. Loureiro Malta, *J. Phys. Chem. C* **2020**, *124*, 10105–10116.

[27] T. N. Nguyen, C. Y. Chow, S. V. Eliseeva, E. R. Trivedi, J. W. Kampf, I. Martinić, S. Petoud, V. L. Pecoraro, *Chem. - A Eur. J.* **2018**, *24*, 1031–1035.

[28] A. N. Carneiro Neto, R. T. Moura, O. L. Malta, *J. Lumin.* **2019**, *210*, 342–347.

[29] E. C. Ximendes, U. Rocha, T. O. Sales, N. Fernández, F. Sanz-Rodríguez, I. R. Martín, C. Jacinto, D. Jaque, *Adv. Funct. Mater.* **2017**, *27*, 1–10.

[30] D. Zhao, J. Zhang, D. Yue, X. Lian, Y. Cui, Y. Yang, G. Qian, *Chem. Commun.* **2016**, *52*, 8259–8262.

[31] L. Zhang, Y. Xie, T. Xia, Y. Cui, Y. Yang, G. Qian, *J. Rare Earths* **2018**, *36*, 561–566.

[32] M. Rodrigues, R. Piñol, G. Antorrena, C. D. S. Brites, N. J. O. Silva, J. L. Murillo, R. Cases, I. Díez, F. Palacio, N. Torras, et al., *Adv. Funct. Mater.* **2016**, *26*, 200–209.

[33] C. Xia, C. Yu, M. Cao, J. Xia, D. Jiang, G. Zhou, D. Zhang, H. Li, *Ceram. Int.* **2018**, *44*, 21040–21046.

[34] H. Wang, D. Zhao, Y. Cui, Y. Yang, G. Qian, *J. Solid State Chem.* **2017**, *246*, 341–345.

[35] D. Ananias, F. A. A. Paz, D. S. Yufit, L. D. Carlos, J. Rocha, *J. Am. Chem. Soc.* **2015**, *137*, 3051–3058.

[36] Z. Wang, D. Ananias, A. Carné-Sánchez, C. D. S. Brites, I. Imaz, D. Maspoch, J. Rocha, L. D. Carlos, *Adv. Funct. Mater.* **2015**, *25*, 2824–2830.